

Supplement of Atmos. Chem. Phys., 15, 9799–9818, 2015  
<http://www.atmos-chem-phys.net/15/9799/2015/>  
doi:10.5194/acp-15-9799-2015-supplement  
© Author(s) 2015. CC Attribution 3.0 License.



*Supplement of*

## **Evaluating BC and NO<sub>x</sub> emission inventories for the Paris region from MEGAPOLI aircraft measurements**

**H. Petetin et al.**

*Correspondence to:* H. Petetin ([herve.petetin@lisa.u-pec.fr](mailto:herve.petetin@lisa.u-pec.fr))

The copyright of individual parts of the supplement might differ from the CC-BY 3.0 licence.

## Supplementary material

### S.1) Determination of the mass-specific absorption coefficient

The Multi-Angle Absorption Photometer (MAAP) instrument provides EBC concentrations deduced from the absorption coefficient measurement converted by a mass-specific absorption coefficient (MAC) of  $6.6 \text{ m}^2 \text{ g}^{-1}$  (Petzold and Schönlinner, 2004). This value had been initially derived from the comparison of 121 ambient EC concentrations measured at one rural background and three traffic impacted urban sites following the German thermal reference method (Schmid et al, 2001; VDI-1 method) with the corresponding MAAP absorption coefficient measurements (at 670 nm). However, considering the high uncertainties that exist on this coefficient, that MAC value may not be adapted to the Paris aerosol. Indeed, while Bond and Bergstrom (2006) have found only slightly variable MAC values for freshly emitted aerosol, around  $7.5 \pm 1.2 \text{ m}^2 \cdot \text{g}^{-1}$  (one sigma confidence) at 550 nm, an enhancement of this coefficient during the transition from external to internal mixing (notably due to organic coatings acting as a prism) has been noticed by several authors based on theoretical models (around +50% in Bond et al., 2006) and laboratory experiments (between +80 and +110% in Schnaiter et al., 2005). It is likely to partly explain the large scatter (up to a factor of 4) of MAC values in ambient conditions (i.e. after a few hours) emphasized by Bond and Bergstrom (2006).

Considering such a large variability of MAC values from one location to the other, one must derive a MAC value relevant for the Paris megacity. A comparison between MAAP absorption coefficient  $b^{(637 \text{ nm})}$  and Sunset Field instrument EC observations (co-located at the LHVP site) is thus performed over the July period. A scatter plot of MAAP versus Sunset observations is shown on Fig. S1. Both are highly correlated ( $R^2$  of 0.88), and the linear regression gives a slope of  $8.8 \pm 0.3 \text{ m}^2 \text{ g}^{-1}$  (at a 95% confidence interval). It is close to the values given by Bond and Bergstrom (2006) for freshly-emitted soot but in the upper range. It is also coherent with the MAC values of  $7.3 \pm 0.1 \text{ m}^2 \text{ g}^{-1}$  obtained during wintertime by Sciare et al. (2011) at Gif-sur-Yvette, a suburban location at 20 km south-west from Paris. Note that the higher (but older) MAC value ( $12.0 \pm 0.7 \text{ m}^2 \text{ g}^{-1}$ ) obtained at Gif-sur-Yvette by Lioussé et al. (1993) may highlight some changes in the soot particles characteristics (e.g. size, shape, organic coating) or more probably reflect the uncertainties associated to the method to determine it (and, in particular, the thermo-optical protocol used to measure EC).

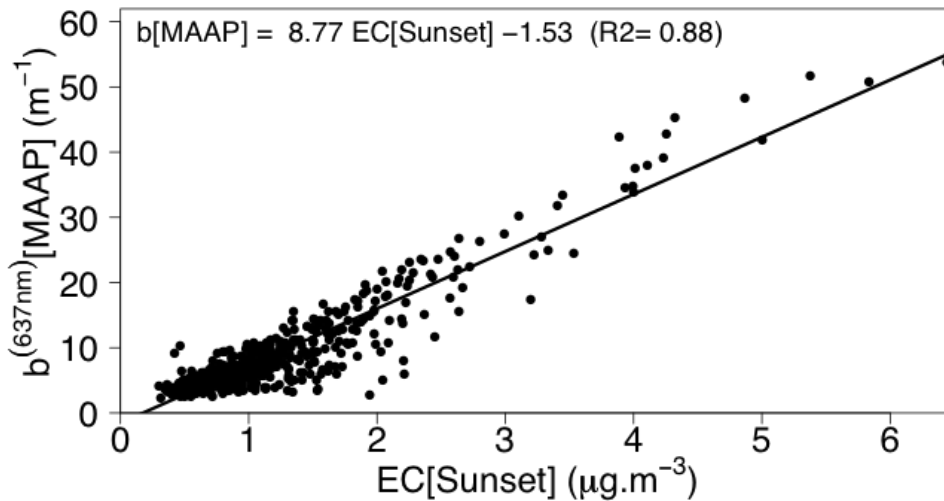


Figure S1 : Hourly MAAP absorption coefficients at 637 nm against Sunset Field EC concentrations at the LHVP site during July.

In addition, there may be discrepancies between the aircraft PSAP and the ground based MAAP instrument. An intercomparison has been performed on July 11 during a few hours, this PSAP giving around 10% higher EBC concentrations, but these results do not appear as representative enough for the whole July month. Müller et al. (2011) have reported PSAP versus MAAP slopes of  $0.79 \pm 0.07$  during the GAW2005 inter-comparison campaign, and  $1.05 \pm 0.08$  and  $0.99 \pm 0.10$  during the EUSAAR2007 one. Applied to our situation, this would lead to a PSAP EBC over Sunset EC ratio between  $1.0 \pm 0.08$  ( $1.27 * 0.79$ ) and  $1.3 \pm 0.13$  ( $1.27 * 1.05$ ). In order to be conservative, that latter value is retained for the MAC uncertainty, thus estimated to 40%.

## S.2) PSAP absorption coefficient measurements

Particles are sampled through an isokinetic and isoaxial aircraft community aerosol inlet (CAI) based on the University of Hawaii shrouded solid diffuser inlet designed by A. Clarke and modified by Meteo France. The CAI inlet allows for entirely sampling the submicron particles and partly sampling of supermicron particles with an upper 50% sampling efficiency for super micron particle sizes at diameter around  $5 \mu\text{m}$  (McNaughton et al., 2007).

The PSAP is then used to measure in near real time the light absorption coefficient. The method is based on the integrating plate technique in which the change in optical transmission of a filter caused by particle deposition is related to the light absorption coefficient of the deposited particles using Beers law. During the MEGAPOLI campaign, the 3 wavelength (467, 530 and 660 nm) version has been operated on board the ATR-42 research aircraft. Several corrections have been applied to the PSAP measurements to obtain absorption coefficients at the three wavelengths and to deduce the BC content from the absorption coefficient extrapolated to 637 nm, thus, comparable to BC derived from state-of-the-art MAAP instruments. The PSAP calibration and correction methods are described in

detail in Bond et al. (1999), Virkkula et al. (2005), and Müller et al. (2011). They include corrections for the PSAP spot size, for aerosol particle scattering (from simultaneous TSI nephelometer measurements) to take into account the decrease in filter transmittance due to scattering, for the absolute transmittance (filters have been changed after every flight, transmittance never decreased below 0.9). The PSAP flow had been calibrated as a function of upstream pressure. From the above described PSAP correction methods, an upper limit of the uncertainty in the derived absorption coefficient has been estimated as 30%.

### **S.3) CHIMERE evaluation of BC, NO<sub>x</sub> and BC/NO<sub>x</sub> at LHVP**

In this section, we evaluate the CHIMERE results at the LHVP ground site against BC and NO<sub>x</sub> observations as well as the BC/NO<sub>x</sub> ratio (see Fig. 6 in the paper).

**Black carbon evaluation.** Observed BC displays a characteristic diurnal profile with a main peak during the morning rush hours, and a more progressive increase at the end of the day. Hourly concentrations range between 0.1-5.7  $\mu\text{g m}^{-3}$ , with a 1.0  $\mu\text{g m}^{-3}$  mean concentration. Highest BC concentrations are observed on July 1, 16, 28 and 29, due to low wind speed conditions, at least in the morning (below  $\sim 1 \text{ m s}^{-1}$  at ground, Fig. 4). Background levels are particularly high on July 1 due to both a clear north-east origin of air masses and a low wind speed, that have allowed a slow and intense BC accumulation in air masses over Northern France and Benelux before reaching Paris. CHIMERE simulations with MM5 data show an overestimation above a factor of 2 whatever the inventory, particularly during morning and evening BL transitions. Largest biases occur with the TNO inventory (NMB of +260%). The meteorology has a significant influence, as shown by the much lower biases obtained with WRF data during evening BL transitions, due to improvements in BLH simulation. In particular, since primary pollutants are highly sensitive to BL dynamics, these improvements lead to significant increase of correlations, approximately from 0.5 to 0.7. Underestimated nighttime BLH with both meteorological models, sometimes associated to low wind speed, is likely to explain some highly overestimated peaks (e.g. 16 July).

**NO<sub>x</sub> evaluation.** Measurements give a mean NO<sub>x</sub> concentration around 22 ppb, with values reaching up to 141 ppb. As expected due to common emission sources with BC, NO<sub>x</sub> compounds show very similar variations, as do model biases. Again, simulations with WRF meteorology give lower concentrations than MM5 ones, leading to reduced but still positive biases for all inventories except EMEP that underestimates NO<sub>x</sub> concentrations. As for BC, both correlation and NRMSE are significantly improved with WRF prediction.

**BC/NO<sub>x</sub> evaluation.** Observed BC/NO<sub>x</sub> ratios remain rather constant over the period, around 0.06  $\mu\text{g m}^{-3} \text{ ppb}^{-1}$  in average. They appear more variable during the night maybe due to higher spatial heterogeneities induced by the lower wind speed and the nocturnal boundary layer stability. In particular, very high peaks observed on July 20 and 25 (up to 0.3  $\mu\text{g m}^{-3} \text{ ppb}^{-1}$ ) may be related to

specific unidentified local BC pollution events in the shallow boundary layer while  $\text{NO}_x$  concentrations are very low. The diurnal profile shows minimum values during the early morning, and a significant increase at the end of the day in observations, due to previously mentioned peaks. Also simulations show rather constant BC/ $\text{NO}_x$  ratios along the day, without any clear diurnal pattern. Ratios are significantly overestimated by the TNO inventory (NMB of +131%) and to a much lesser extent by the EMEP inventory (+67%), while a low bias is obtained with the TNO-MP inventory (+13%). The influence of dynamics is mostly removed, as attested by the quite similar results with both MM5 and WRF meteorological data. All these discrepancies between inventories are consistent with the discussion in Sect. 3.2 (Fig. 2).

Table S1 : Statistical results on BC ( $\mu\text{g m}^{-3}$ ),  $\text{NO}_x$  (ppb) and BC/ $\text{NO}_x$  ratio ( $\mu\text{g m}^{-3} \text{ppb}^{-1}$ ) at the LHVP site.

Species	Case	NMB		NRMSE		N	
		MB	(%)	RMSE	(%)	R	(%)
BC	EMEP (MM5)	+1.1	+93	2.0	170	0.42	99
	TNO (MM5)	+3.1	+260	4.5	372	0.39	99
	TNO-MP (MM5)	+1.3	+110	2.3	191	0.43	99
	EMEP (WRF)	+0.5	+43	1.3	106	0.70	99
	TNO (WRF)	+2.2	+187	3.7	312	0.67	99
	TNO-MP (WRF)	+0.7	+59	1.6	135	0.70	99
$\text{NO}_x$	EMEP (MM5)	+1.0	+5	23.6	108	0.40	96
	TNO (MM5)	+7.8	+36	26.8	122	0.40	96
	TNO-MP (MM5)	+12.8	+58	30.8	141	0.38	96
	EMEP (WRF)	-5.4	-25	15.7	72	0.77	96
	TNO (WRF)	+0.8	+4	17.2	78	0.72	96
	TNO-MP (WRF)	+4.8	+22	19.8	90	0.71	96
BC/ $\text{NO}_x$	EMEP (MM5)	+0.04	+67	0.05	87	0.22	95
	TNO (MM5)	+0.08	+131	0.09	146	-0.15	95
	TNO-MP (MM5)	+0.01	+13	0.03	56	0.17	95
	EMEP (WRF)	+0.04	+72	0.06	90	0.23	95
	TNO (WRF)	+0.08	+136	0.09	150	-0.07	95
	TNO-MP (WRF)	+0.01	+11	0.03	55	0.19	95

#### S.4) LHVP site representativeness

In order to assess the area impacting results obtained at the LHVP site, a simulation is performed over 5 days (1-5 July) in which NO<sub>x</sub> emissions at various distances from the site from 0 to 33 km are colored by inert tracers (Fig. S2). Tracer emission rates are taken from the TNO inventory. For simplification, no diurnal profile is assigned to these emissions, but this is not expected to modify results since most of emissions share the same diurnal variability (associated to the dominant traffic source). From this approach, it is possible to determine the contribution of emissions at a given distance to the concentration at the LHVP site.

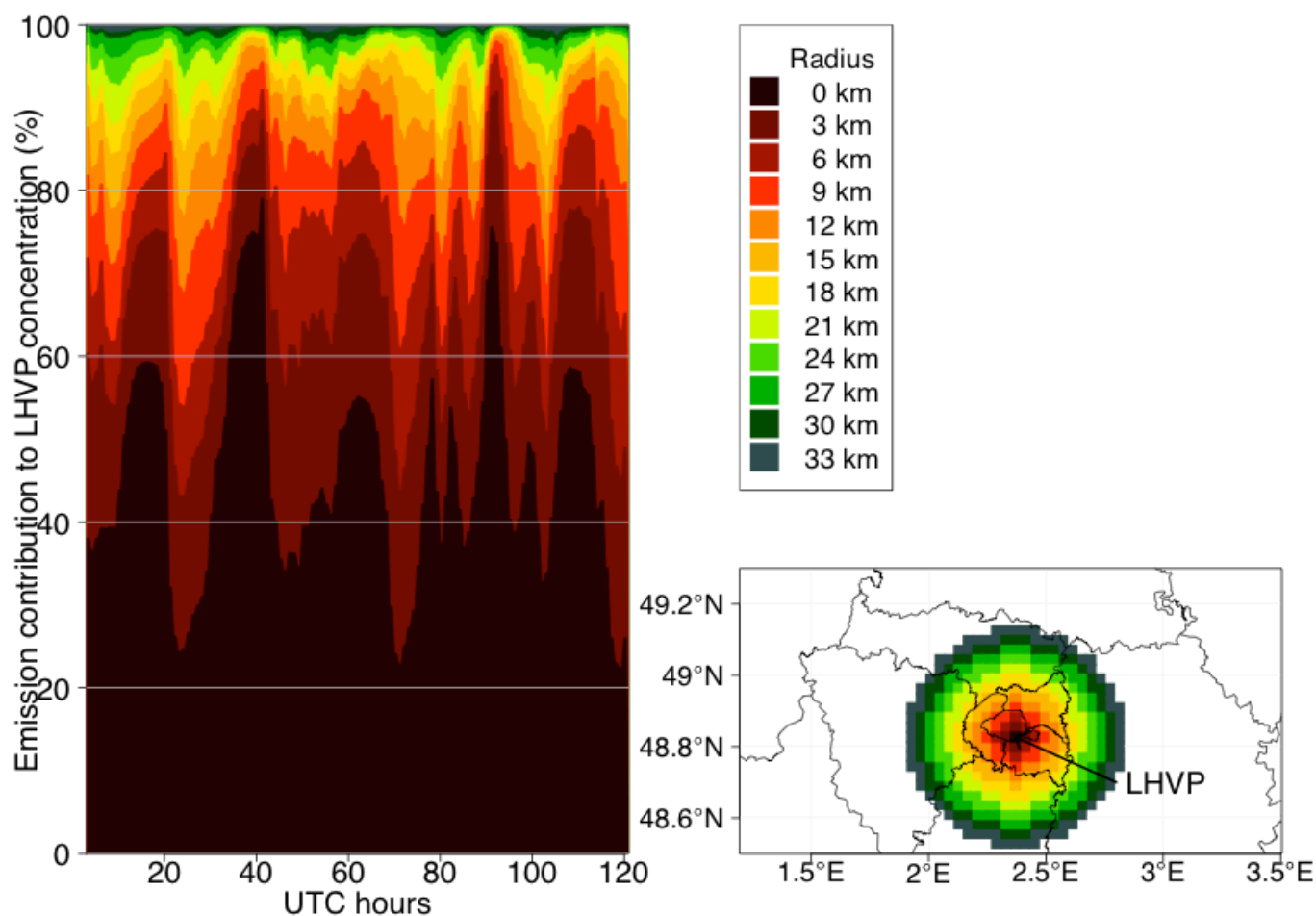


Figure S2 : Emission contributions to LHVP concentrations at several distances from the site (left panel) and map of these emissions (right panel). Distances are those of the centers of the grid points.

As expected, the largest contribution originates from emissions in the cell where LHVP is located. It is quite variable in time with values ranging from 25 to 75%, notably depending on the wind, with highest values (at hour ~90) associated to stagnant conditions (wind speed below 1 m.s<sup>-1</sup>). Conversely, the most distant emissions beyond 21 km contribute to less than

10%. These results indicate that emission error factors obtained at LHVP are strongly influenced by nearby sources and are not representative for the whole agglomeration.

## S.5) Supplementary figures and tables

Table S2 : July BC emissions in the Ile-de-France region.

SNAP sector	Description	July factor*	July emissions (tons)		
			EMEP	TNO	TNO-MP
1	Public electricity and other energy transformation	0.234	1	2	2
2	Small combustion plants	0.261	22	77	18
3	Industrial combustion and processes with contact	0.939	4	6	1
4	Industrial process emissions	1.026	7	30	9
5	Fossil fuel production	1.001	7	0	0
6	Solvent and product use	1.077	2	2	0
7	Road transport	1.029	353	316	234
8	Other non-road transport and mobile machinery	1.030	131	57	22
9	Waste disposal	1.000	3	50	2
10	Agriculture	0.593	0	0	0
Total		-	530	540	288

\*For each SNAP sector: [July emission] = [annual emission]\*[July factor]/12

Table S3 : Wind speed statistical results during flight days, between 6:00-14:00 UTC, in the altitude range of 110-210 m, for MM5 model (and WRF in parenthesis).

July day	Mean observation (m s <sup>-1</sup> )	NMB (%)	NRMSE (%)
9	7.03	+3.2 (+3.1)	23 (13)
10	6.36	+1.9 (+9.0)	12 (18)
13	5.08	-21 (-34)	25 (36)
15	9.14	+0.51 (-6.1)	12 (9.4)

16	3.69	-34 (-39)	44 (47)
21	7.55	+12 (+2.7)	32 (26)
25	6.31	+5.3 (-3.2)	12 (11)
28	3.83	-17 (-46)	31 (58)
29	4.42	+27 (+8.8)	29 (19)
All	5.93	-0.27 (-8.0)	24 (25)

---

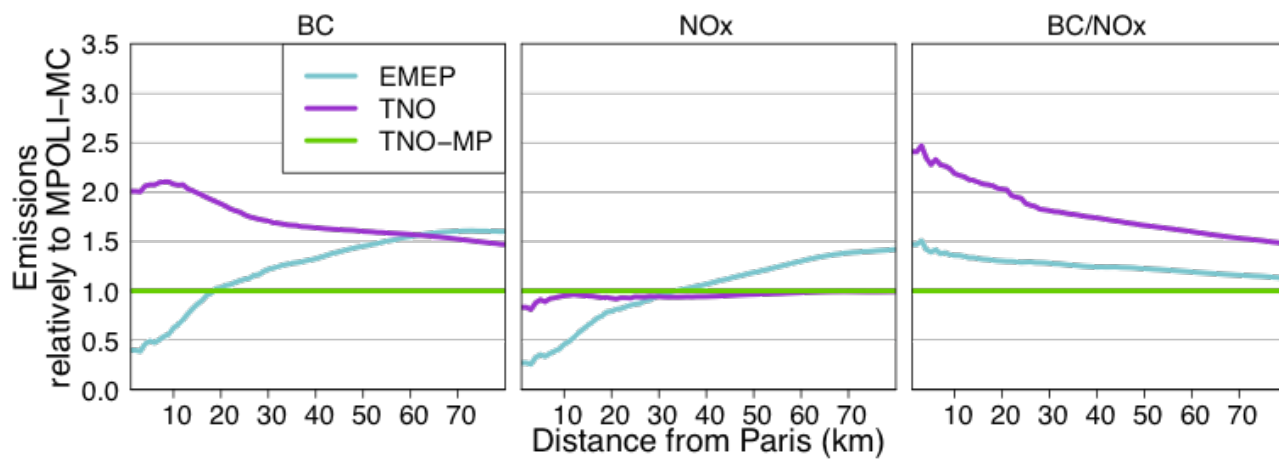


Figure S3 : Integrated BC, NO<sub>x</sub> and BC/NO<sub>x</sub> emissions at various distances from the LHVP site, relatively to the TNO-MP inventory.

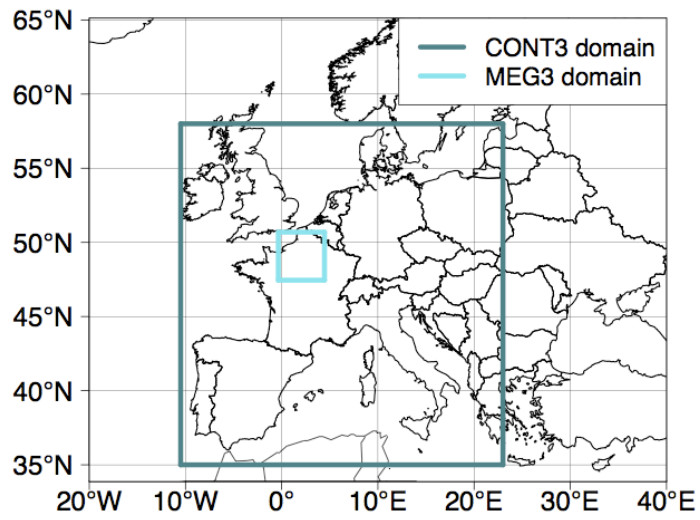


Figure S4 : Nested domains.

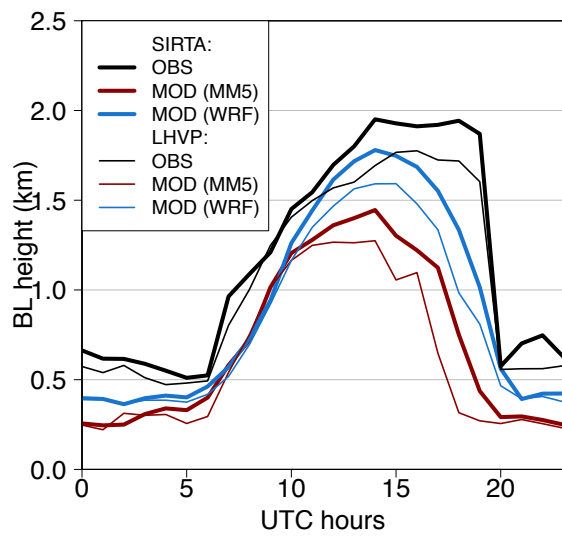


Figure S5 : Observed and simulated diurnal profile of BLH at SIRTA and LHVP sites.

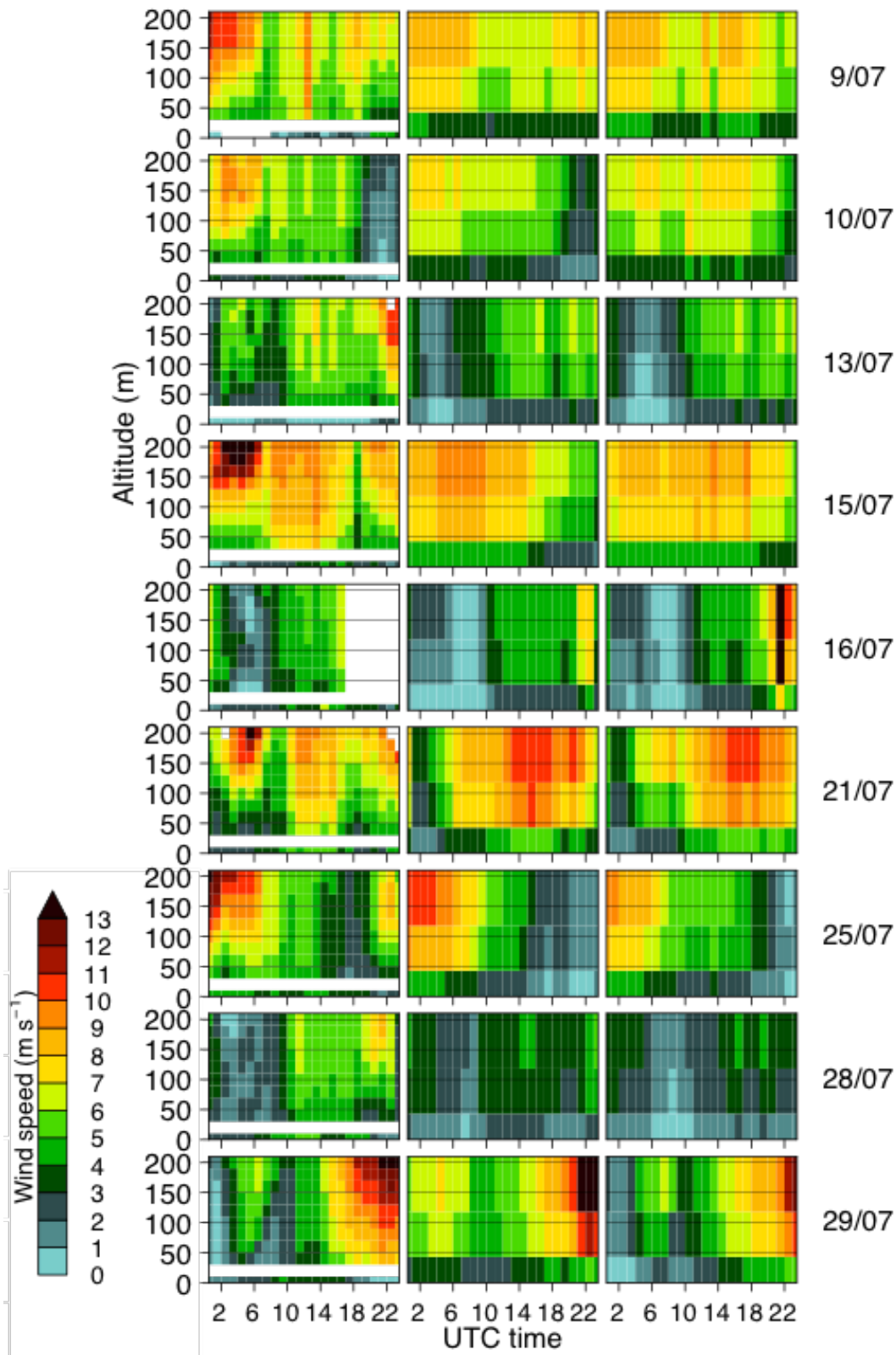


Figure S6 : Hourly wind speed at various altitudes (above ground) at the SIRTA site for each flight day (no available data for the 1 July), from Lidar observations (left column), MM5 (middle column) and WRF model simulations (right column). Previously discussed wind speed observations at ground are also reported in the left column.

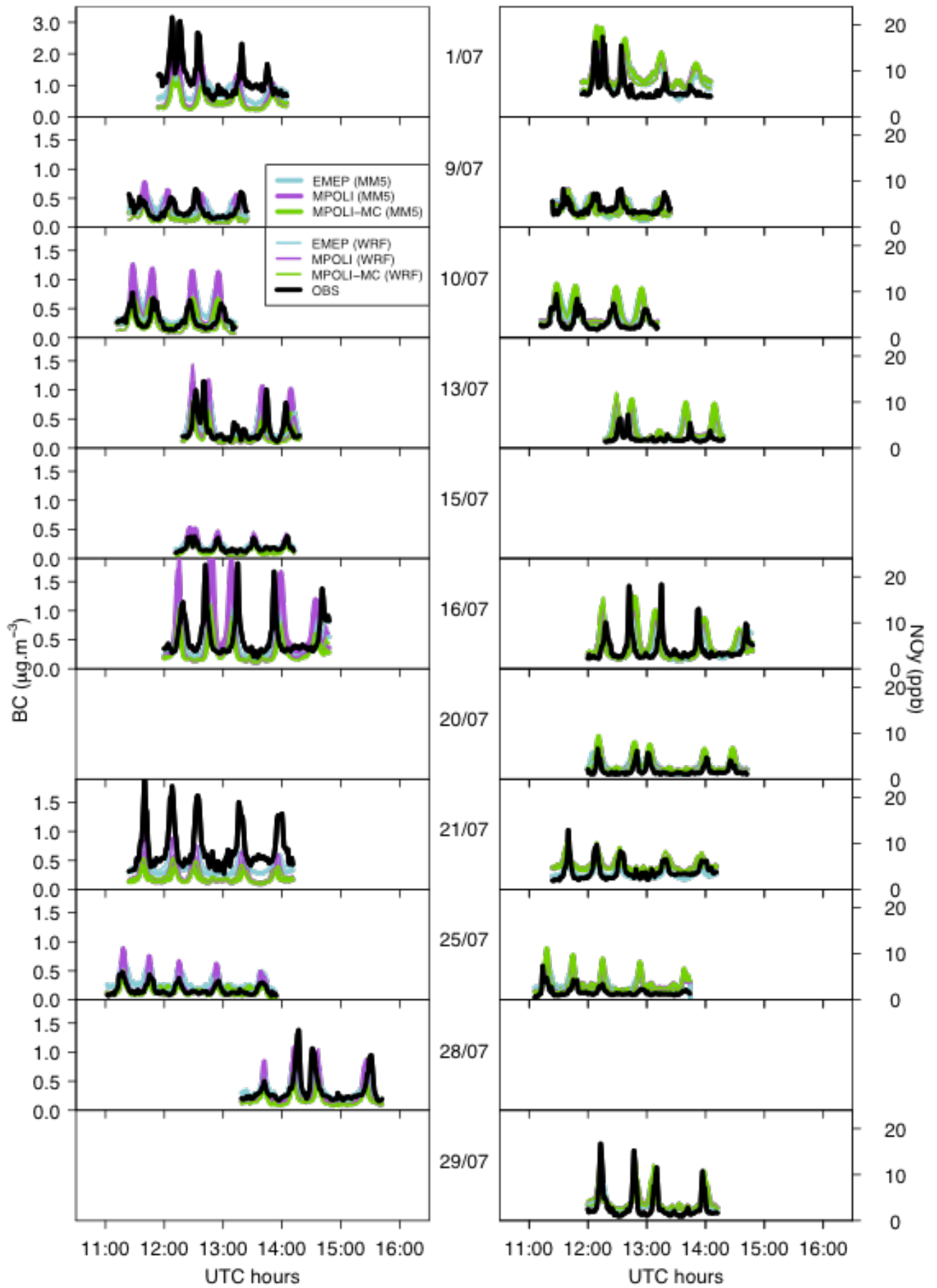


Figure S7: Observed and simulated BC (left column) and NO<sub>y</sub> (right column) concentrations along aircraft trajectories, for each flight.

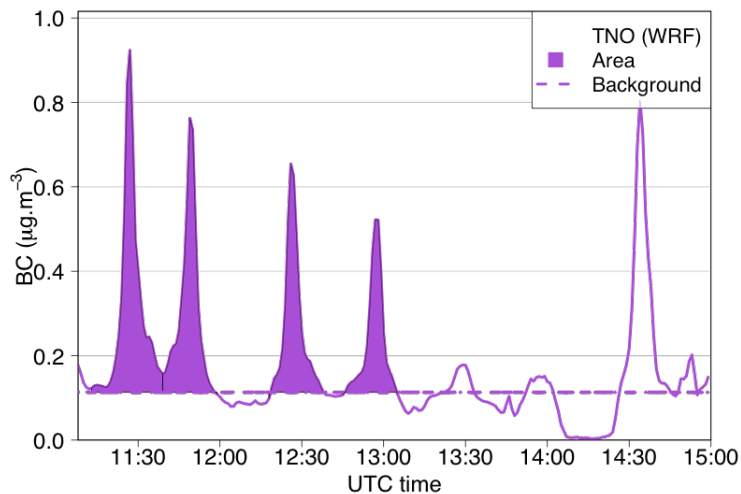


Figure S8 : Peak integral (purple area) above background (dotted line) for the TNO/WRF simulation the 10 July.

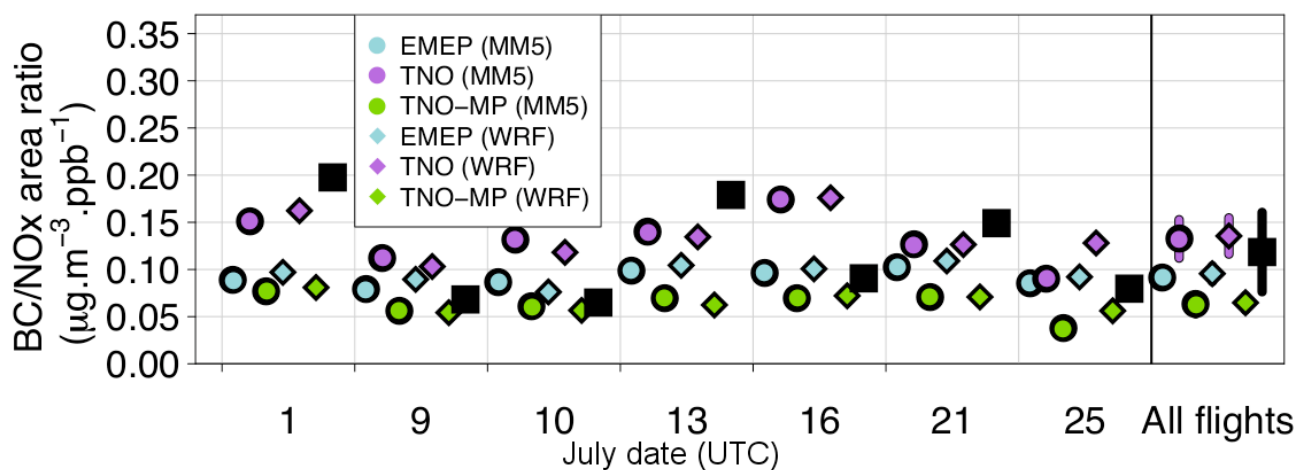


Figure S9: Ratio of the BC over  $\text{NO}_y$  peak area for observations and simulations.

Table S4 : BC/ $\text{NO}_x$  mean results.

Meteorological data	Inventory	Mean bias	Uncertainty factor	Confidence interval
MM5	EMEP	-18%	1.41	(-42%; +16%)
	TNO	+7%	1.41	(-24%; +50%)
	TNO-MP	-46%	1.34	(-60%; -28%)
WRF	EMEP	-18%	1.36	(-40%; +12%)
	TNO	+13%	1.36	(-17%; +53%)

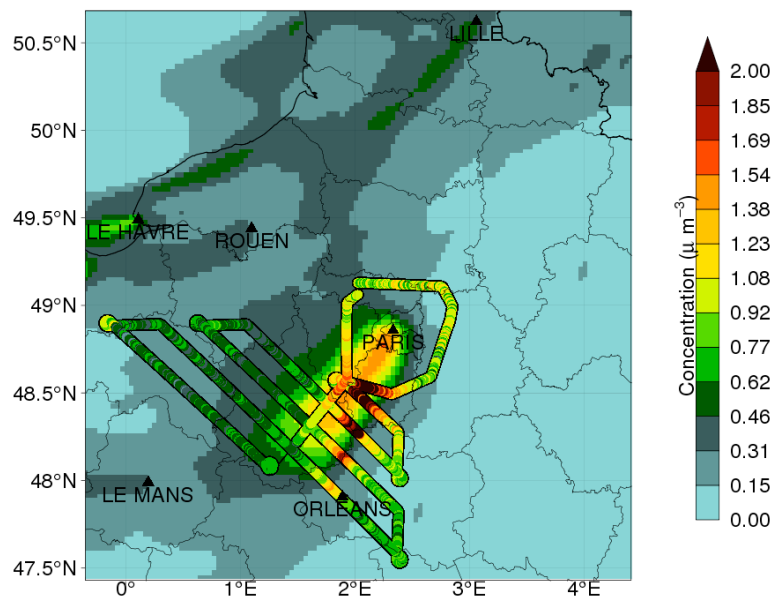


Fig. S10 : Aircraft trajectory and observed (along the trajectory) and modeled (in background, with the TNO-MM5 case) BC concentration for the 1 July.

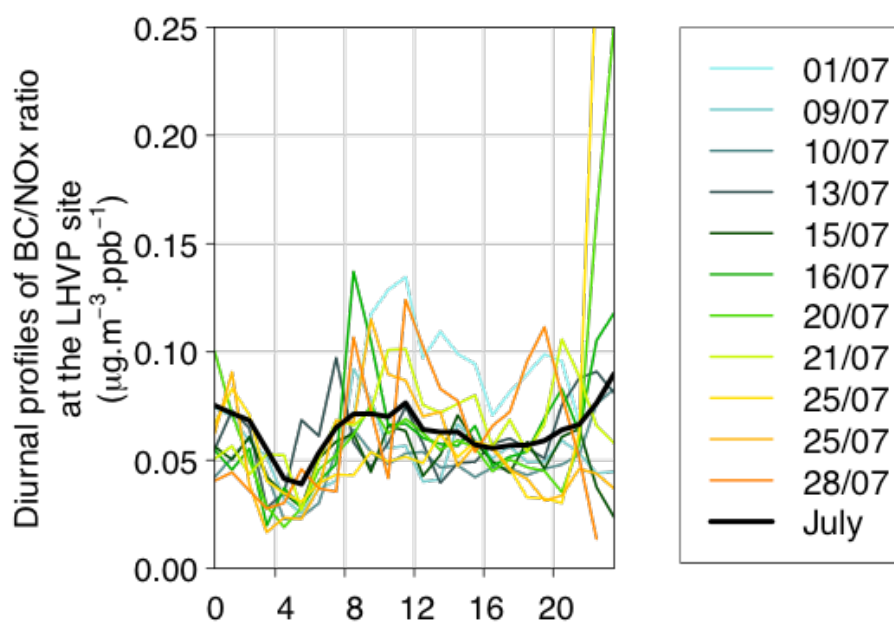


Figure S11 : BC/NO<sub>x</sub> ratio diurnal profiles for each flight day and in average over the whole July month at the LHVP site.

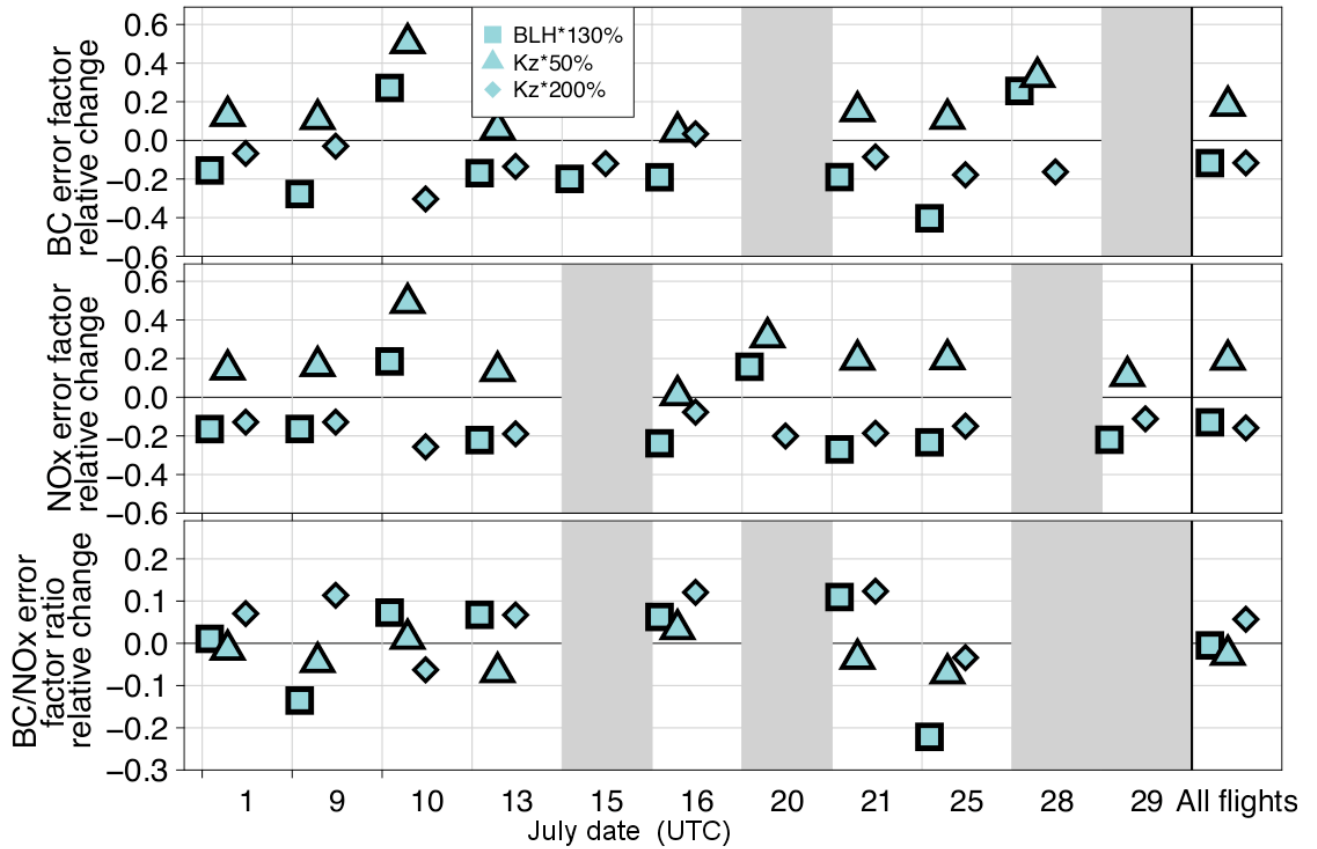


Figure S12 : BC and NO<sub>x</sub> emission error factors relative changes with modified K<sub>z</sub> and BLH (and EMEP/TNO-MP taken as reference) for MM5 meteorology.

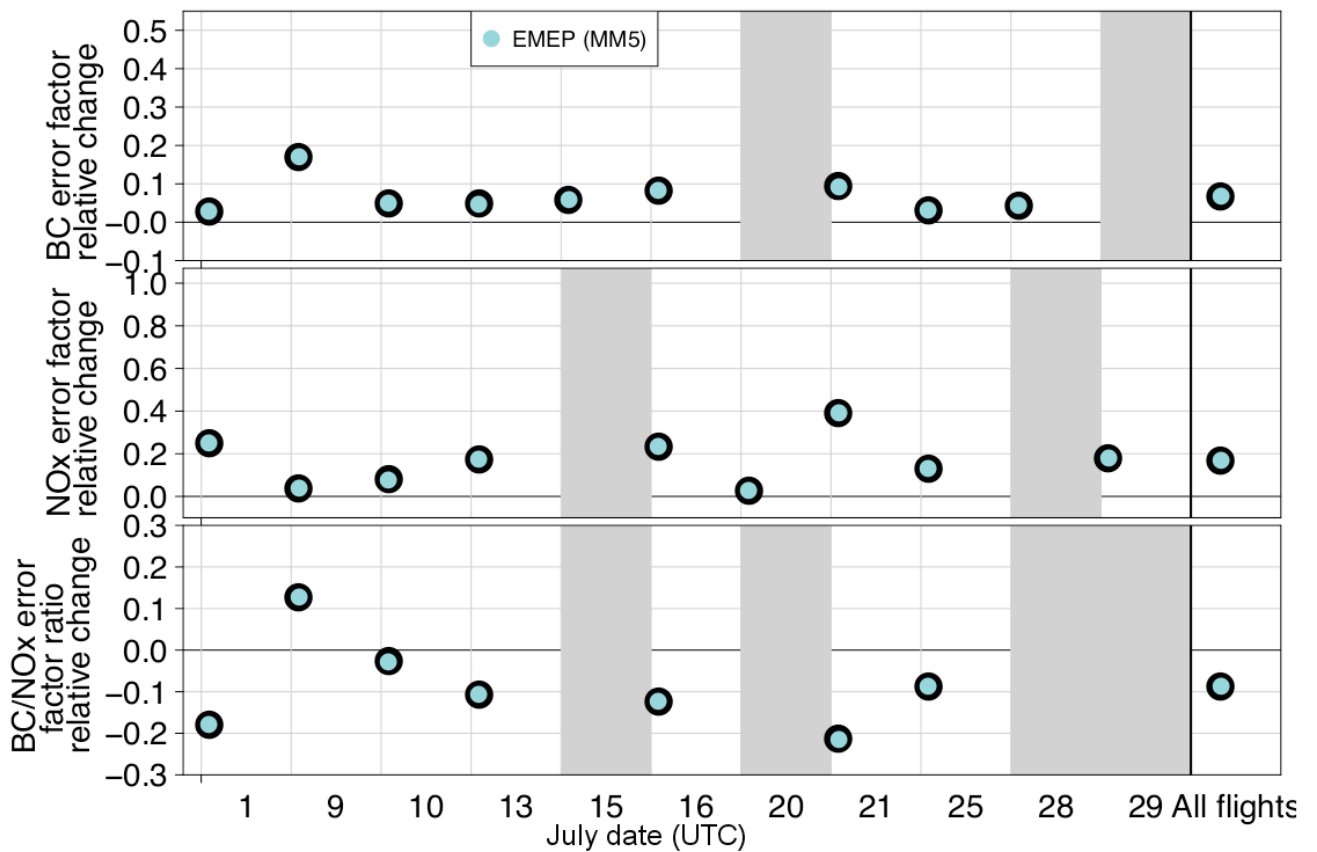


Figure S13 : BC, NO<sub>x</sub> error factor and BC/NO<sub>x</sub> error factor ratio changes after removing any deposition on both species (note that the scale is no longer logarithmic).

## S.6) Additional references

- Bond, T. C. and Bergstrom, R. W. : Light Absorption by Carbonaceous Particles : An Investigative Review, *Aerosol Sci. Tech.*, 40, 27–67, 2006.
- Bond, T. C., Habib, G., and Bergstrom, R. W. : Limitations in the enhancement of visible light absorption due to mixing state, *J. Geophys. Res.*, 111, 2006.
- Müller, T., Henzing, J. S., de Leeuw, G., Wiedensohler, A., Alastuey, A., Angelov, H., Bizjak, M., Collaud Coen, M., Engström, J. E., Gruening, C., Hillamo, R., Hoffer, A., Imre, K., Ivanow, P., Jennings, G., Sun, J. Y., Kalivitis, N., Karlsson, H., Komppula, M., Laj, P., Li, S.-M., Lunder, C., Marinoni, A., Martins dos Santos, S., Moerman, M., Nowak, A., Ogren, J. A., Petzold, A., Pichon, J. M., Rodriguez, S., Sharma, S., Sheridan, P. J., Teinilä, K., Tuch, T., Viana, M., Virkkula, A., Weingartner, E., Wilhelm, R., and Wang, Y. Q. : Characterization and intercomparison of aerosol absorption photometers : result of two intercomparison workshops, *Atmospheric Measurement Techniques*, 4, 245–268, 2011.
- Petzold, A. and Schönlinner, M. : Multi-angle absorption photometry - a new method for the measurement of aerosol light absorption and atmospheric black carbon, *J. Aerosol Sci.*, 35, 421–441, 2004.
- Schmid, H., Laskus, L., Abraham, H. J., Baltensperger, U., Lavanchy, V., Bizjak, M., Burba, P., Cachier, H., Crow, D., Chow, J., Gnauk, T., Even, A., ten Brink, H. M., Giesen, K.-P., Hittenberger, R., Hueglin, C., Maenhaut, W., Pio, C., Carvalho, A., Putaud, J.-P., Toom-Sauntry, D., and Puxbaum, H. : Results of the "carbon conference" international aerosol carbon round robin test stage I, *Atmos. Environ.*, 35, 2111–2121, 2001.
- Schnaiter, M., Lücke, C., Möhler, O., Naumann, K.-H., Saathoff, H., Wagner, R., Schurath, U., and Wehner, B. : Absorption amplification of black carbon internally mixed with secondary organic aerosol, *J. Geophys. Res.*, 110, 2005.